Jacob Elms[1]
Department of Earth and Environmental Sciences,
University of Manchester,
Manchester M139PL, UK
e-mail: jacob.elms@manchester.ac.uk

Alison Pawley
Department of Earth and Environmental Sciences,
University of Manchester,
Manchester M139PL, UK
e-mail: alison.pawley@manchester.ac.uk

Nicholas Bojdo
Department of Mechanical, Aerospace and Civil Engineering,
University of Manchester,
Manchester M139PL, UK
e-mail: nicholas.bojdo@manchester.ac.uk

Merren Jones
Department of Earth and Environmental Sciences,
University of Manchester,
Manchester M139PL, UK
e-mail: merren.a.jones@manchester.ac.uk

Rory Clarkson
Rolls-Royce plc.,
Derby, DE24 8BJ UK
e-mail: rory.clarkson@rolls-royce.com

Formation of High-Temperature Minerals From an Evaporite-Rich Dust in Gas Turbine Engine Ingestion Tests

The ingestion of multi-mineral dusts by gas turbine engines during routine operations is a significant problem for engine manufacturers because of the damage caused to engine components and their protective thermal barrier coatings. A complete understanding of the reactions forming these deposits is limited by a lack of knowledge of compositions of ingested dusts and unknown engine conditions. Testbed engines can be dosed with dusts of known composition under controlled operating conditions, but past engine tests have used standardized test dusts that do not resemble the composition of the background dust in the operating regions. New evaporite-rich test dust was developed and used in a full engine ingestion test, designed to simulate operation in regions with evaporite-rich geology, such as Doha or Dubai. Analysis of the engine deposits showed that mineral fractionation was present in the cooler, upstream sections of the engine. In the hotter, downstream sections, deposits contained new, high-temperature phases formed by the reaction of minerals in the test dust. The mineral assemblages in these deposits are similar to those found from previous analyses of service returns. Segregation of anhydrite from other high-temperature phases in a deposited sample taken from a high-pressure turbine blade suggests a relationship between temperature and sulfur content. This study highlights the potential for manipulating deposit chemistry to mitigate the damage caused in the downstream sections of gas turbine engines. The results of this study also suggest that the concentration of ingested dust in the inlet air may not be a significant contributing factor to deposit chemistry. [DOI: 10.1115/1.4050146]

Keywords: turbomachinery, erosion & deposition, dust ingestion test, CMAS, sulfidation, mineral dusts, harsh environments, measurement techniques, turbine blade and measurement advancements

Introduction

The design of aircraft gas turbine engines is generally optimized based on operation in clean air. To improve the efficiency of fuel burn, modern-day turbofans are made with increasingly tight tolerances and are pushed to work with ever-increasing peak gas temperatures. Yet in many cases, the air they breathe contains significant quantities of atmospheric aerosols that can cause damage to the internal surfaces of the engine. In recent decades, the number of aircraft operating in such environments has increased in parallel with the rise of service contracts between the airline and the engine supplier, resulting in the transfer of risk and ultimately cost of the damage incurred. This has led to engine manufacturers paying much closer attention to the deleterious effects that result from the ingestion of these atmospheric agents.

Mineral dusts constitute 70% of the global aerosol mass burden [1]. They are complex mixtures of different minerals, and they exhibit significant regional, spatial and temporal variation in mineral fraction and particle size distribution [2]. If ingested into an aircraft engine, they may erode, corrode, or build up as a surface deposit within the core of the gas turbine engine, causing a reduction in blade efficiency and restrictions along the flow path.

Mineral dust concentrations in the air are highest during seasonal dust storms (e.g., $\sim 10^3$ μg m^{-3} [3]), but background concentrations are still significant (e.g., $\sim 10^1$–10^2 μg m^{-3} [4]): under these conditions, a turbofan engine with a design point core mass flow rate of 100 kg s^{-1} may ingest 0.1–10 g s^{-1} of dust during the take-off run. Ingested dust will interact with the engine in many different ways, including colliding with high-speed rotating blades, becoming trapped in between blades and shrouds, glazing combustor walls, or depositing on to nozzle guide vanes. Combined with the changing contractual relationship between the engine supplier and end user, this has led to increased efforts by original equipment manufacturers (OEMs) and researchers in recent years to investigate the relationship between the resultant damage and the characteristics of the ingested dust. In many of these studies, analogs have been developed to resemble the natural conditions and used to simulate ingestion events. One such effort was the *sand and dust ingestion tests* conducted by Rolls-Royce in spring 2018 using new test dust, produced by the University of Manchester on the engine manufacturer's behalf. The tests were designed to understand the chemistry of engine deposits formed in a region where the surface geology contributes significant quantities of evaporite and calcium carbonate minerals to the ingested dust. The current work presents some of the findings from these tests. The results identify a number of key gaps in the research area and have important implications for the future mitigation of damage to gas turbine engines.

Background

There are a great number of experimental and numerical studies on the process of particle damage to gas turbine engines.

[1]Corresponding author.
Contributed by the International Gas Turbine Institute (IGTI) of ASME for publication in the Journal of Turbomachinery. Manuscript received September 18, 2020; final manuscript received January 7, 2021; published online April 7, 2021. Assoc. Editor: David G. Bogard.

Table 1 A summary of minerals present in ex-service aircraft engine deposits reported 1993–2009

Authors	Component (engine type)	Minerals identified	Reported operating region
de Wet et al. [12]	High pressure turbine (HPT) blade (unspecified)	Anhydrite and diopside	Middle East
Smialek et al. [13]	Turbine disc cooling passage (turboshaft)	Anhydrite and quartz	Persian Gulf
Smialek et al. [13]	Turbine vane (turboshaft)	Diopside and quartz	Persian Gulf
Borom et al. [14]	First stage turbine shroud (turboshaft)	Diopside	Saudi Arabia
Braue [15]	HPT blade cross section (unspecified)	Anhydrite, melilite, wollastonite, spinel, and perovskite	Unspecified

A comprehensive review of these works is given by Suman et al. [5]. However, very few of the studies that focus on engine deposits from ingested mineral dust describe the deposit chemistry in terms of the minerals present, instead only report the bulk chemistry. This is significant because without identifying the minerals present it is not possible to determine what reactions have taken place. Many minerals become unstable at high temperatures and can react together to form new secondary phases in the hot sections of gas turbine engines. These secondary phases may include a melt that may permeate thermal barrier coating (TBC) lamellae and attack the underlying substrate [6,7]. Deposits may also contain sulfur compounds such as calcium or sodium sulfate that can react with the nickel super-alloy in a process known as sulfidation [8–10]. In this process, sulfur can infiltrate and degrade the alloy, reducing its corrosion resistance, strength, and structural integrity [11]. While substantial work has been done on the effect of $CaO–MgO–Al_2O_3–SiO_2$ (CMAS) melts on TBCs, only a handful of studies have speculated on the role of the ingested mineral dust in the development of this damage and investigated the formation of secondary phases through the analysis of surface deposits. This work can be broadly split into two groups: analysis of in-service engine parts and analysis of components intentionally damaged during full engine sand and dust ingestion tests.

Analysis of Service Returns. Several previous studies have included chemical analysis of deposits found in engines returned from service in dusty environments, as summarized in Table 1 [12–15].

These authors' results (Table 1) are significant because they indicate the presence of high-temperature minerals such as diopside ($CaMgSi_2O_6$), spinel ($MgAl_2O_4$), melilite [$Ca_2(Mg,Al)(Al,Si)SiO_7$], and wollastonite ($CaSiO_3$) that are either uncommon or not present in natural mineral dusts but are known to form by high-temperature reactions of CMAS compositions [16]. The inference is that these must have formed in the engine. However, the detection of minerals that form outside of the CMAS system—such as perovskite ($CaTiO_3$) and anhydrite ($CaSO_4$)—demonstrates that the bulk chemistry of deposits and their formative reactions are more complex than that of a purely quaternary CMAS system. Moreover, most of the high-temperature minerals detailed in Table 1 can incorporate elements other than CMAS in their structure. For example, melilite can be represented as $(Ca,Na)_2(Mg,Al,Fe^{2+})(Al,Si)SiO_7$ and so (if present in the deposit) Fe^{2+} and Na may contribute to melilite chemistry.

Understanding the reactions that form these high-temperature minerals requires quantitative knowledge of the chemistry of the ingested mineral dust. In a non-experimental setting, this is most easily established where the aircraft type under investigation is a rotorcraft, which develops its own intense dust cloud from the local ground surface with its downwash [13]. In contrast, fixed-wing aircraft engines—that have much longer maintenance timescales and fly long distances across regions of contrasting parent geology—do not often incur their damage from dust sourced from a single location or during a single event. As a consequence, uncertainty in the mineral composition of the dust ingested over time, and its cumulative effect on the chemistry of the deposits in the engine, limits the current understanding of the transformations taking place through the engine.

Whole Engine Sand and Dust Ingestion Tests. The effects of natural mineral dusts on the components of gas turbine engines have also been studied in experimentally simulated dust ingestion events, using testbed engines and synthetic mixtures of mineral dusts of known particle size distribution and composition ("test dusts") [17]. An example of a commonly used commercial test dust is Arizona test dust, which is mainly comprised of SiO_2- and Al_2O_3-rich minerals [18]. Arizona test dust is widely used in tests including durability testing of gas turbine engines [19]. Dusts of different compositions have been developed to address specific damage mechanisms that are not recreated when Arizona test dust is used. For example, to reproduce glassification in engine hot sections (as observed after the ingestion of volcanic ash), Dunn et al. produced a blend of two types of soil (Hollywood sand and Corona clay), Mount St. Helens' volcanic ash and Wyoming bentonite [19]. Other dusts, such as AFRL03 (34 wt% quartz, 30 wt% gypsum, 17 wt% aplite, 14 wt% dolomite, and 5 wt% halite [20]), have been optimized to form CMAS-like deposits on hot section components and maximize the melt infiltration of TBCs [17].

As the focus of this study was to understand the chemistry of engine deposits formed during flight through a source region containing significant evaporite and calcium carbonate minerals, a new test dust representative of that composition was required. As the composition and particle size distribution of the test dust are known, its evolution as it passes through and deposits in the cold and hot sections of a modern commercial development engine can be fully characterized.

Methods

New test dust (TD50) was produced at the University of Manchester and developed in collaboration with Rolls-Royce. The formulation of TD50 was based on known compositions of natural mineral dusts that exist in arid Middle Eastern regions with high air traffic. Dubai, for example, is the third busiest commercial passenger airport in the world [21].

Middle Eastern mineral dust is comprised of variable amounts of quartz, feldspars, carbonates (calcite and dolomite), micas, clay minerals, evaporite minerals, and oxides [22]. Although the bulk chemistries of airborne Middle Eastern dusts are similar, the mineral composition varies locally. This reflects the composition and moisture content of the surface sediment (e.g., carbonate-rich soils, alluvium, and dried-out, ephemeral saline lakes or "playas"), type of vegetation cover, and atmospheric processes [2,22]. The test dust produced in this study is more representative of areas with higher carbonate and evaporite mineral content.

A fine-skewed, unimodal grain-size distribution (D = particle diameter: $D_{50} = 14\ \mu m$ and $D_{90} = 47\ \mu m$) was mixed from ten individually prepared mineral powders. The approximate composition of TD50 is shown in Fig. 1.

A complete turbofan engine was used for the tests to ensure that minerals in the ingested dust behaved in the same way as they would when ingested on-wing.

Rolls-Royce Dust Ingestion Tests. Dust ingestion tests were specified and performed by Rolls-Royce using a modern turbofan development engine previously used in European testbeds, but not in dusty environments. TD50 was delivered at engine air inlet

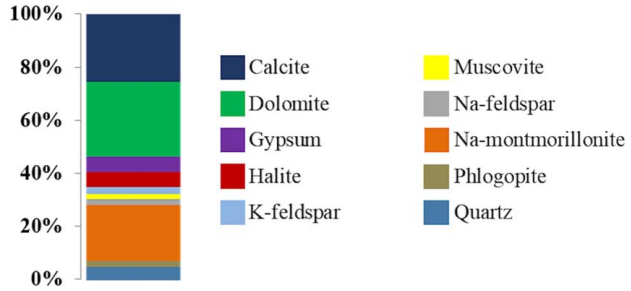

Fig. 1 Approximate mineral composition of TD50. Trace minerals (not shown) are cristobalite, kaolinite, illite, and pyrite.

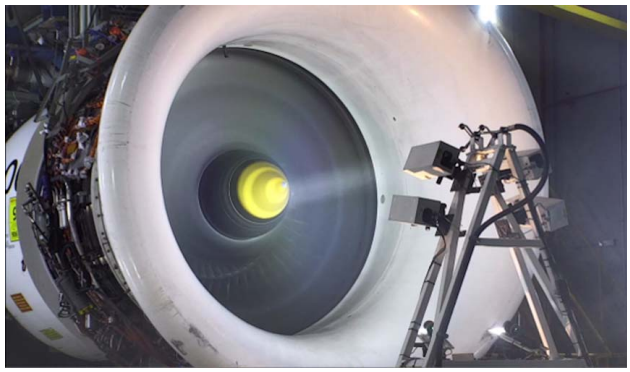

Fig. 2 Rolls-Royce dust ingestion test setup at engine inlet, showing dust delivery system

velocity and room temperature using the engine test equipment setup shown in Fig. 2. Eight tests were performed in total, over a range of durations (10–30 min), concentrations of TD50 (0–10 mg m^{-3}) and calculated turbine inlet temperatures (TIT, 1350 ± 14 or 1450 ± 15 °C) as detailed in Fig. 3. All other stated temperatures were directly measured using thermocouples to an uncertainty of ±0.5%.

The engine was instrumented with temperature and pressure sensors in each section of the engine. Between each test, the degree of deposition in the combustor and turbine sections was monitored using a borescope.

After the tests were completed, the engine was completely stripped to enable sampling of sections and components. Deposits that formed on components throughout the different stages of the engine were sampled and analyzed using a range of techniques to determine their chemistry.

Sampling Protocol. Samples of deposits were taken by Rolls-Royce engineers from the engine components and sections of the engine during the engine strip using brushes, scalpels, and spatulas. A wide range of sample locations were selected to determine the progressive distribution and reactions of the primary minerals as they traveled through primary and secondary air systems of the engine and deposited on internal surfaces. The samples described here were removed from the intermediate pressure compressor (IPC), combustor (C), high-pressure nozzle guide vane (HPNGV), and high-pressure turbine (HPT) sections and are listed in Table 2. Their locations in the engine are shown in Fig. 4. All samples (except HPT1) were analyzed by powder X-ray diffraction (XRD) to determine their mineral composition. HPT1 was analyzed by scanning electron microscopy/energy-dispersive X-ray spectroscopy to investigate the distribution of phases within the sample. It was removed from the blade as a glassy flake and then cut perpendicular to the blade surface to reveal a cross section of the deposit at this location.

X-Ray Diffraction. A Bruker pXRD machine equipped with a D8 Advance diffractometer was used to collect the diffraction patterns of the samples. Phases were assigned using database patterns in the EVA (Bruker DIFFRAC.EVA) program package and quantified by Rietveld analysis using TOPAS (Bruker DIFFRAC.TOPAS) software. The detection limit for assigning phases has been previously measured at around 1 wt%, and the

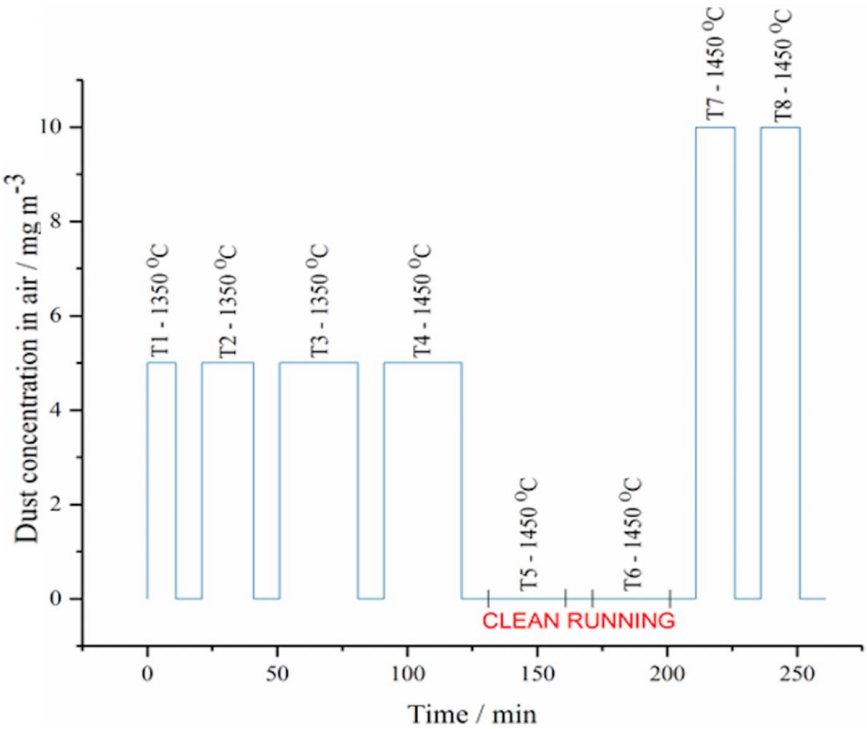

Fig. 3 Rolls-Royce dust ingestion test plan

Table 2 Samples removed during engine strip-down

Engine section	Sample number	Description
IPC	IPC1	Shroud
	IPC2	Hub (pressure side)
	IPC3	Blade mid-span (suction side)
Combustor	C1	Combustor wall (burner)
	C2	Combustor wall (cooling holes)
HPNGV	HPN1	Vane aerofoil
	HPN2	Inner side platform (hub)
HPT	HPT1	Blade shroud underside (pressure side)
	HPT2	Blade shank (suction side)

uncertainty in quantification of proportions is typically around 2 wt %. Multiple measurements were made to ensure repeatability.

Scanning Electron Microscopy With Energy-Dispersive X-Ray Spectroscopy. Backscattered electron (BSE) images and energy-dispersive X-ray spectroscopy (EDX) maps and spectra of HPT1 were collected using an FEI (Field Electron and Ion Company) Quanta 650 scanning electron microscope that is equipped with a field emission gun. The sample was mounted in an epoxy resin block and polished sequentially to 0.25 μm before carbon coating by a vaporized carbon method.

Results and Discussion

Engine Borescoping. Borescoping of the engine before the test showed that the internal surfaces were clean and free of debris, as shown in Fig. 5(*a*). Images taken after dust ingestion testing (Figs. 5(*b*)–5(*f*)) show that large deposits formed throughout the primary air sections of the engine from the ingested mineral particles. Clean running of the engine resulted in the shedding of some of the deposits from the hot section components but substantial quantities of deposited material remained, as shown in Figs. 5(*d*) and 5(*e*). Subsequent disassembly of the engine identified that dust had infiltrated the majority of the engine, forming deposits in both the primary air system and secondary air systems. Deposits ranged from physisorbed, fine mineral dust particles in the coolest section (air: 40 °C) to chemisorbed glasses in the hottest section (air: 1400 °C). The scale of dust infiltration in the test engine highlights a key gap in the research area, as while the effects of mineral dust deposition have been widely studied in the primary gas flow, those in the secondary air system—such as the chemical interactions between deposits and nickel super-alloy components—have been rarely considered.

Composition of Upstream Deposits. Quantified XRD analysis (Fig. 6) identified that the IPC samples IPC1, IPC2, and IPC3 were composed of test dust minerals with a range of concentrations. A particularly high concentration (55 wt%) of aluminum was also identified in IPC1 (taken from the IPC shroud) and is likely indicative of the ingested dust causing erosion damage to upstream components such as the abradable compressor lining. Aluminum has been excluded from IPC1 in Fig. 6, and the mineral concentrations have been scaled accordingly to facilitate complete comparison between the test dust and the IPC samples.

A simple way to compare the average mineral composition at the IPC to that of TD50 (Fig. 6) is by percentage difference. The largest compositional differences are halite (~300% TD50), gypsum (~210% TD50), muscovite (~160% TD50), and Na-montmorillonite (~120% TD50), which are enriched in the average IPC composition relative to TD50. These large enrichments are facilitated by the depletion of quartz (~90% TD50), calcite (~80% TD50), and dolomite (~20% TD50) in the average IPC deposit composition relative to TD50. The changes in mineral proportions between TD50 and the IPC samples are most likely to be caused by the different behaviors of each mineral in the flow, as explained in the following section.

Mineral Fractionation in the Compressor. Variation in mineral concentration at the three different locations in the compressor correlates with differences in mineral shape. Test dust minerals with a platy shape (such as Na-montmorillonite and muscovite) were found to be abundant at the hub (IPC2) and shroud (IPC1) in comparison with the mid-span (IPC3) of the blade. In comparison, halite, which has a cubic shape, was found to be significantly more abundant at the mid-span location over the hub and shroud.

The shape and size of particles change their aerodynamic properties and so may lead to separation and sorting within the compressor of minerals with different inherent sphericities ("mineral

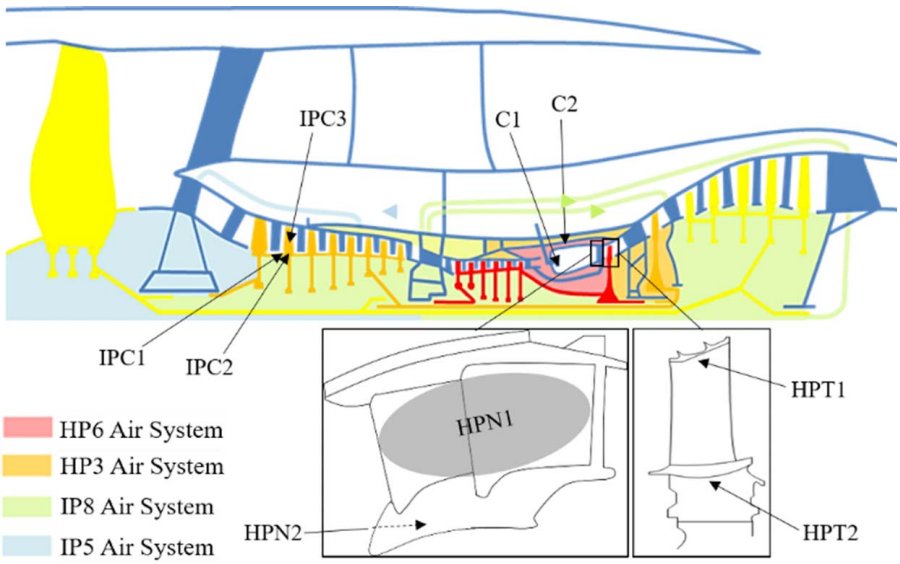

Fig. 4 Simplified turbofan engine cross section. Sampled deposit locations are indicated with arrows and secondary air systems are labeled using color. Arrowheads indicate the direction of flow: HP, high-pressure compressor; IP, intermediate pressure compressor.

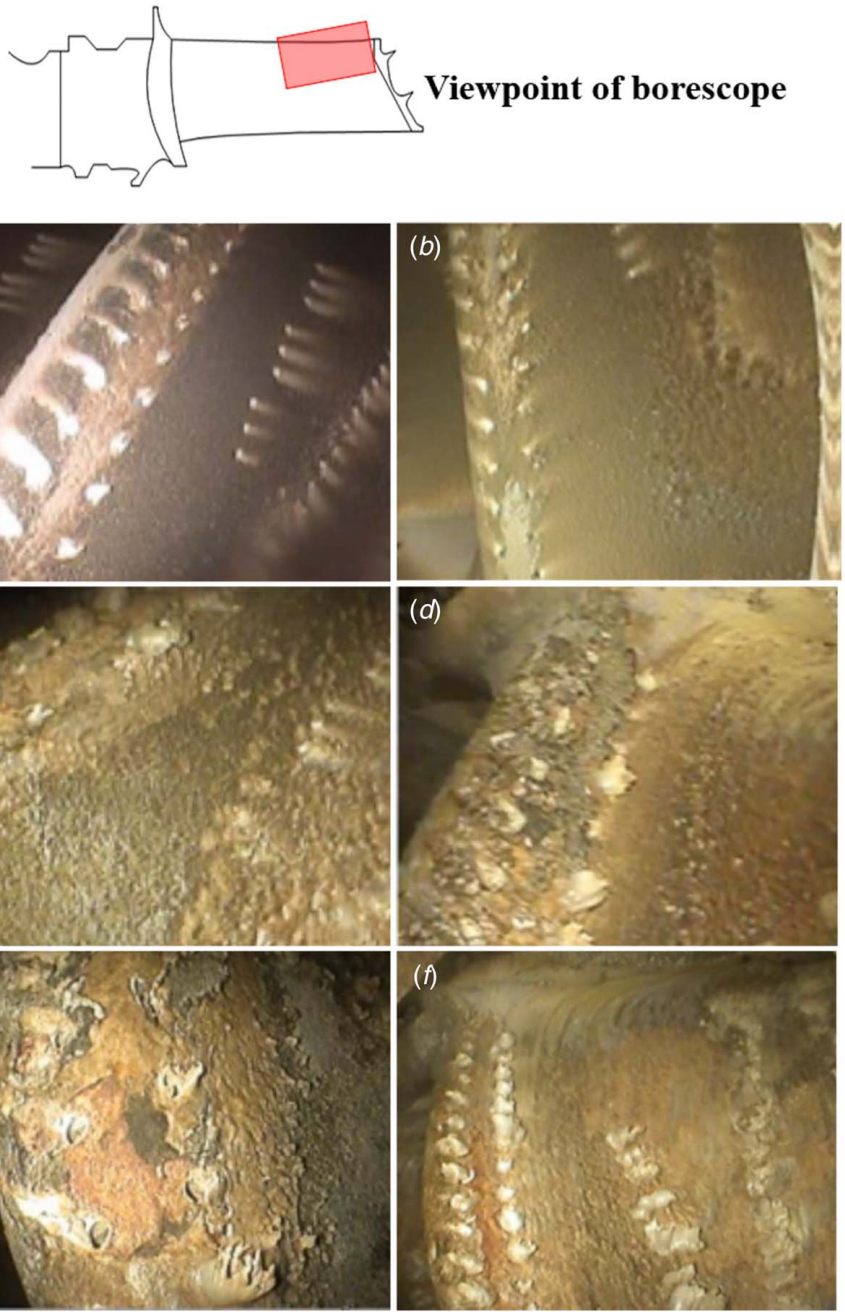

Fig. 5 Borescope images of high-pressure turbine, taken of the same blade: (*a*) before testing, (*b*) post test 3, (*c*) post test 4, (*d*) and (e) post clean running, and (*f*) post test 8. The part of the blade shown in the borescope images is indicated in the above schematic.

fractionation"). Sphericity (or shape factor) is defined by Ghenaiet [23] as the ratio of the surface area of a sphere to the surface area of a non-spherical particle of equivalent volume.

Particles entrained within the main axial flow of the compressor may either follow the main flow path over the blade, deposit on the blade aerofoil (IPC3), or become entrained in turbulent secondary flows and deposit at either the base (IPC1 and IPC2) or tip of the blade. Less spherical or more irregular particles with a lower value of shape factor will have a higher drag coefficient at a given particle Reynolds number and so will follow fluid streamlines more closely than a spherical particle [24]. Therefore, the platy Na-montmorillonite and muscovite are more likely to either follow the main flow over the blade or become entrained in secondary flows around the base of the blade and deposit, as observed in IPC1 and IPC2. The more spherical halite particles are more likely to deviate from the flow and deposit on the mid-span of the blade, as observed at IPC3.

In the context of deposit chemistry, understanding mineral fractionation in these upstream sections is important because it influences the minerals that may deposit and react in the upstream sections of gas turbine engines. While a further in-depth discussion of mineral fractionation is out of scope for this study, future work will assess the role of particle morphology (size and shape) in deposition probability at distinct sites in the engine.

Composition of Downstream Deposits. Samples C1, C2, HPN1, and HPT1 were taken from primary flow deposits in the

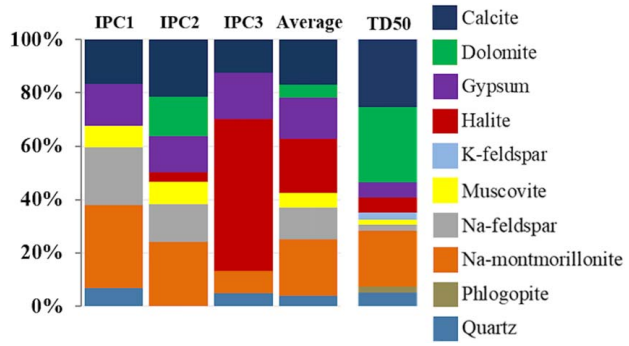

Fig. 6 XRD quantification of minerals present in IPC samples: shroud (IPC1), hub (IPC2), blade mid-span (IPC3), and the average composition of the IPC. TD50 composition is shown for comparison.

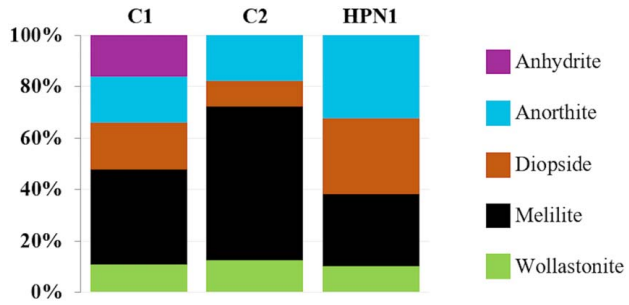

Fig. 7 XRD quantification of minerals present in combustor (C1 and C2) and HPNGV (HPN1) deposit samples from locations in the primary flow. Quartz present in HPN1 (<1 wt%) is not shown.

highest temperature sections of the engine: the combustor, HPNGV, and HPT (air = 1015–1400 °C), as shown in Fig. 4 and described in Table 2.

Quantified XRD analysis of C1, C2, and HPN1 (Fig. 7) identified that melilite (28, 37, and 60 wt%), wollastonite (10, 11, and 12 wt %), diopside (10, 18, and 29 wt%) and anorthite ($CaAl_2Si_2O_8$: 18, 18, and 32 wt%) were present in all three samples. Very low amounts of quartz (SiO_2, <1 wt%) were present in sample HPN1, and C1 was found to contain an appreciable concentration of anhydrite (16 wt%). All three samples contained glass, which was observed on their XRD patterns as a characteristic broad amorphous hump.

Samples were also taken from deposits located in the secondary air system of the HPNGV and HPT (air = 540–620 °C, samples HPN2 and HPT2) bled from the combustor and the high-pressure compressor (HPC) primary air. XRD analysis identified some of

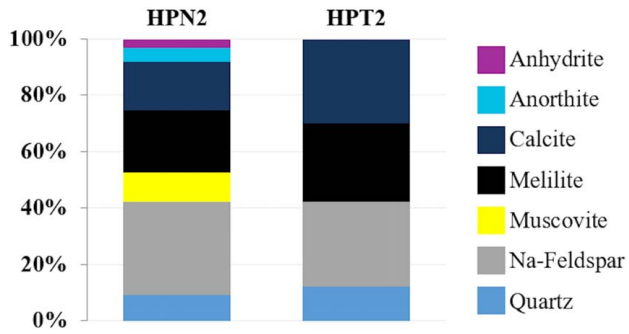

Fig. 8 XRD quantification of minerals present in HPNGV (HPN2) and HPT (HPT2) deposit samples from locations in the secondary air system

the same minerals as their primary flow counterparts, as shown in Fig. 8. Both samples contained melilite (22 and 28 wt%) and quartz (9 and 12 wt%), and anorthite (5 wt%) and anhydrite (3 wt %) were present in HPN2. In addition to quartz, other minerals present in the test dust—muscovite (10 wt%), calcite (17 and 30 wt%), and Na-feldspar (33 and 30 wt%)—were identified in HPN2 and HPT2, contrasting with primary flow counterparts HPN1 and HPT1.

The formation of new phases in these high-temperature deposits is the result of deposit composition and temperature, variables that are best illustrated by describing the liquidus and solidus behavior of CMAS. The scaled bulk CMAS composition of TD50 is plotted on Fig. 9, which is a $CaO–Al_2O_3–SiO_2$ liquidus projection onto the 10% MgO plane. Bulk CMAS compositions of engine deposit samples from the studies of Borom et al. [14] and Braue [15] have been calculated from the average compositions reported and are also plotted on Fig. 9. TD50 plots in the melilite field of primary crystallization on Fig. 9 (as does the bulk composition of Borom et al. [14]), and so it follows that melts of dusts derived from TD50 crystallize melilite at their liquidus temperature around 1300 °C. Adjacent minerals join the crystallizing assemblage as the temperature decreases toward the solidus temperature, where the last drop of melt crystallizes. The work of Osborn et al. [16] demonstrates the CMAS composition of TD50 plots in the anorthite, wollastonite, diopside, and melilite solidus field at 1210 °C, and so below this temperature, these four phases will form. As both glass (derived from a melt) and these four crystalline phases are present in the primary flow samples, the temperatures of these deposits must have been between the liquidus and solidus temperature. C1 may have been closer to the solidus temperature than the other samples because it contains a relatively high concentration of anhydrite, which begins to decompose around 1225 °C [27]. At its location on the burner, C1 was exposed to a mixture of primary and secondary flows in the form of pre- and post-combustion air, and so this may have caused it to be at a lower temperature than the other primary flow samples. The temperature of the secondary air system was much lower than that

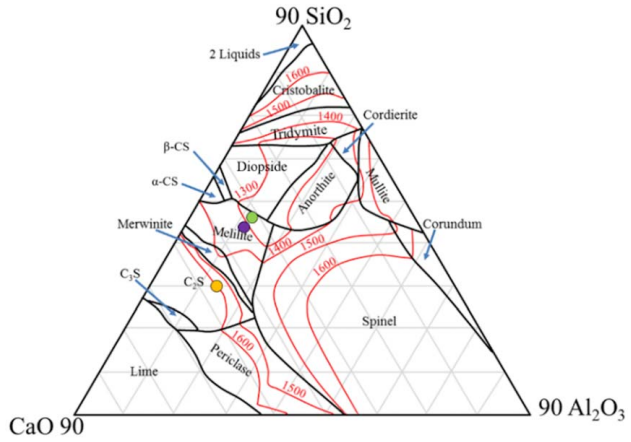

Key	Author	CaO	Al_2O_3	SiO_2	MgO
	Borom (1996)	32	12	49	7
	Braue (2009)	44	13	29	13
	Test Dust 50 (this study)	35	12	43	10

Fig. 9 $CaO–Al_2O_3–SiO_2$ liquidus projection onto the 10% MgO plane. Labels show the solid phase in equilibrium with the liquid at liquidus temperature. Boundaries of primary phase fields are indicated and liquidus temperature contours are labelled with their corresponding temperature. The reported compositions of Borom (1996), Braue (2009), and this study are plotted and scaled for a pure CMAS system in the 10% MgO plane. Projection redrawn from Ref. [25] using the data of Refs. [14,15,26].

Table 3 EPMA of representative melilites in C1

Oxides	Oxide composition/wt%		
	M1	M2	M3
SiO_2	44.4	32.9	43.6
Al_2O_3	5.6	17.9	7.0
FeO[a]	0.3	1.5	0.6
MgO	10.3	7.5	9.6
CaO	36.7	39.3	35.2
Na_2O	2.9	0.7	3.3
Trace[b]	0.3	0.2	0.3
Total	100.5	100.0	99.6

[a]All Fe analyzed as Fe^{2+}.
[b]Trace oxides are TiO_2, Cr_2O_3, MnO, K_2O, ZrO_2, SO_3, and P_2O_5.

of the primary air, and so it is not unexpected that the four-phase assemblage is absent in HPN2 and HPT2. The lower temperature of these deposits is also likely to be the reason that the test dust minerals calcite, Na-feldspar, and muscovite were identified in HPN2 and HPT2 but not the primary flow samples, as at elevated temperatures these minerals would become unstable. Compared to the other test dust minerals, quartz is more stable at elevated temperatures and so it follows that it was identified in deposits from both air systems.

Electron Probe Microanalysis of Melilite. Melilite dominates the chemistry of the hot section deposits in this study as it is both the primary mineral to crystallize from TD50-derived melts and one of the four crystalline phases that are present at the solidus temperature. Electron probe microanalysis (EPMA) of sample C1 (Table 3) found that melilite formed a range of solid solution compositions between its end members alumoåkermanite [$CaNaAl(Si_2O_7)$], gehlenite [$Ca_2Al(AlSiO_7)$], and åkermanite [$Ca_2Mg(Si_2O_7)$].

In nature, melilite is present in silica-undersaturated igneous rocks such as nephelinites or calcium-aluminum-rich inclusions (CAIs) in carbonaceous chondrite meteorites [28,29]. The melilite compositions in Table 3 are enriched in Na_2O but depleted in Al_2O_3 in comparison to CAI melilites such as those studied by Grossman [28]. The characteristically aluminum-rich bulk chemistry of CAIs plot in the spinel field of primary crystallization in Fig. 9 and experimental studies have found that spinel is the first phase to crystallize [30] rather than melilite. In this respect, the melilites in Table 3 are more similar to igneous melilites, such as those studied by Gee and Sack [29] and Melluso et al. [31]. However, as the test dust contained low amounts of FeO, the melilites of this study are depleted in iron relative to these natural igneous melilites.

The chemistry of the melilites in this study—along with that of the other phases formed in the hot section deposits—is controlled by that of the test dust. All of the new phases are predominantly calcic because of the high concentrations of calcium-bearing carbonate minerals in the test dust. As suggested in previous work, increasing the content of stable high-temperature crystalline phases reduces the amorphous content and reduces the depth of melt infiltration of the TBC [32,33]. Melilite is, therefore, of particular interest because of the variety of elements that it can incorporate and stabilize at the high temperatures of the hot section.

Sulfur Segregation Effect in Hot Section Deposits. An interesting finding from the scanning electron microscopy with energy-dispersive X-ray spectroscopy (SEM/EDX) analysis of sample HPT1 (location described in Table 2 and Fig. 4) was the segregation of sulfur from other major elements. As outlined in the Introduction, the origin and behavior of sulfur within engine deposits is particularly important to study because of the damage it can cause to metallic components through sulfidation corrosion. EDX mapping and point analysis of HPT1 found that sulfur was segregated toward the blade surface edge of the sample. These sulfur-rich

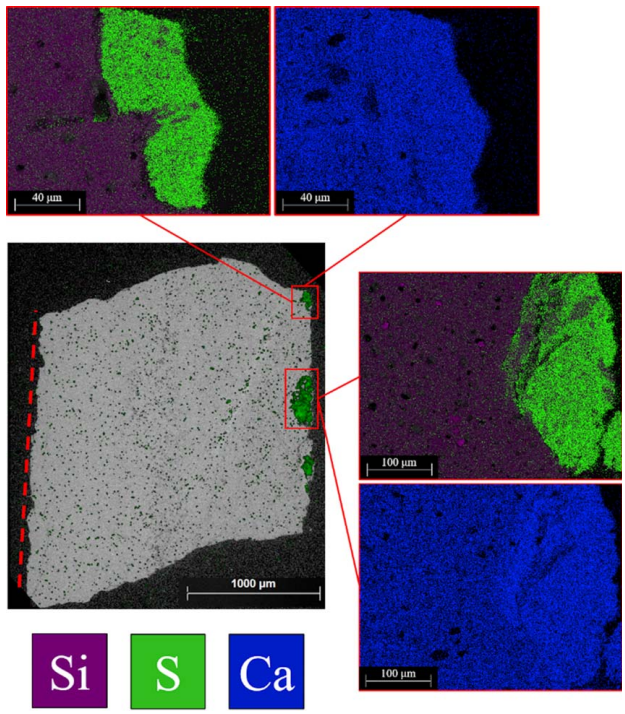

Fig. 10 BSE overlaid sulfur and silicon EDX maps and calcium EDX map of sample HPT1. Edge exposed to hot gas flow indicated with a dashed line.

regions were also calcium-rich but depleted in all other major elements in the sample (Mg, Al, Si, and Na), as indicated by the silicon EDX map in Fig. 10. Anhydrite was previously identified in the XRD analysis of samples C1 and HPN2 in this study, and so is likely to be the dominant phase present in these segregated regions.

As indicated in Fig. 10, the band containing sulfur was closest to the blade surface and furthest from the hot gas flow. This is likely to be the cooler side of the deposit due to the cooling of the blade relative to the hot exhaust gas stream and so there appears to be a relationship between sulfur content and temperature. As the chemistry of the other hot section samples has suggested that they were between their liquidus and solidus temperatures, HPT1 is also likely to have been partially molten under the operating conditions of the engine. Any sulfur present in hotter regions is likely to have been lost from the melt by volatilization, whereas in cooler regions anhydrite appears to have been stabilized as a solid phase. It is unclear whether anhydrite formed directly by the dehydration of gypsum in the test dust or precipitated from the melt at the cooler interior of the deposit, following the reaction of SO_2 in the exhaust gases with calcium in the melt. In the latter case, calcium in the precipitated anhydrite would be provided not only by the gypsum in the test dust but also by the other calcium-rich phases. If anhydrite had formed *via* this mechanism, there may be a link between calcic minerals such as calcite and the propagation of sulfidation damage. Further investigation of this effect is the subject of the current work.

Conclusions

Dust ingestion testing of a gas turbine engine using TD50 has provided a number of key observations that link the chemistry of the ingested dust to the complex mineral deposits that form:

(1) Pronounced variation in the concentration of mineral phases was observed in upstream deposits, and downstream deposits contained a variety of high-temperature phases.

(2) Melilite, wollastonite, diopside, and anorthite were identified in deposits sampled from high-temperature locations in the primary flow. As these minerals have been previously identified in deposits taken from ex-service engines, this implies that the test dust and test methodology realistically simulated the conditions of natural ingestion events.
(3) Mineral fractionation was evident in samples of deposits formed in different locations in the IPC and will be largely determined by the transport behavior of each mineral in the flow. Physical properties of the minerals, such as shape and size, are highly influential on the transport behavior and can be readily controlled through the use of test dusts.

As the chemistry of the ingested dust, the fractionation behavior of individual minerals and the chemistry of deposits are all known variables in this study, it is possible to speculate on the origins of the new phases formed in the hot section. For example, calcite and dolomite were found to be depleted from their test dust concentrations in comparison with other TD50 minerals deposited at the IPC, and calcite was identified in deposits from regions in the secondary air system bled from the HPC. As both must have been present in the mineral fraction that reached the combustor and are likely to be the main sources of calcium and magnesium for these deposits, their presence is likely to be critical to the chemistry of these deposits.

The observation of anhydrite in the hot section suggests that it may have formed in the high-temperature molten deposits from the reaction of calcium with dissolved sulfate species. In one of the turbine deposit samples (HPT1), anhydrite was found to be segregated from other phases at the cooler, blade surface edge of the sample. This suggests that there is a relationship between the sulfur content and the local temperature of the sample.

Our results illustrate the range in the chemistry of the stable crystalline phases—such as melilite—that can form in high-temperature deposits. The exploitation of this range in chemistry has the potential to reduce the damage that high-temperature deposits cause to engines. In addition to the damage caused by the infiltration of TBCs, molten deposits containing calcium could precipitate sulfates that may proliferate sulfidation corrosion. Sodium in deposits has also been proposed to contribute to corrosion mechanisms [10,34]. As a stable, high-temperature crystalline phase, melilite effectively "locks-up" these elements and may reduce their ability to cause damage in the hot section of the engine. Propagation of the crystallization of high-temperature minerals such as melilite in hot section deposits could, therefore, provide a route to limiting both corrosion and TBC damage and so effectively mitigate some of the issues caused by dust ingestion. Investigation of the employment of this approach will be the subject of future work.

It is important to note that the concentrations of dust in the air in these tests were particularly high, similar to heavy dust storms such as "Red Dawn" [35]. Tests were designed in this way to assess whether similar phases and damage to in-service examples could be produced over short test durations, which are necessary due to fueling requirements. High dust concentrations led to large deposit build-up (as discussed previously), and so it was possible to investigate and observe the effect of deposit shedding during clean runs by borescoping the engine. Repeated ingestion events of low concentrations of dust are the most significant because of their regularity, but the chemistry of the deposits may in fact be independent of the initial concentration of the bulk dust ingested. As the chemistry of the deposits (along with other effects such as shedding) has been found in this study to be similar to that of deposits formed in the engines of service aircraft, it is reasonable to suggest that this experimental approach was suitable.

Acknowledgment

This research was supported by an EPSRC M4DE CDT PhD studentship (EP/L01680X/1), sponsored by Rolls-Royce, to Elms and an EPSRC IAA grant 207 (EP/K502947/1) to Jones, Bojdo, and Pawley. We would like to thank the following for their help with the various chemical analyses: Kate Brodie (SEM), Heath Bagshaw (SEM), John Waters (XRD), Jon Fellowes (EPMA), and Lewis Hughes (SEM). We would like to acknowledge the efforts of staff at Rolls-Royce who ran the engine tests and collected the samples. We are grateful to Antonio Filippone for their support and Stephen Covey-Crump for the constructive advice on mineralogy.

Conflict of Interest

There are no conflicts of interest.

Data Availability Statement

The data sets generated and supporting the findings of this article are obtainable from the corresponding author upon reasonable request. The authors attest that all data for this study are included in the paper. No data, models, or code were generated or used for this paper.

References

[1] Ryder, C. L., Marenco, F., Brooke, J. K., Estelles, V., Cotton, R., Formenti, P., McQuaid, J. B., Price, H. C., Liu, D., Ausset, P., Rosenberg, P. D., Taylor, J. W., Choularton, T., Bower, K., Coe, H., Gallagher, M., Crosier, J., Lloyd, G., Highwood, E. J., and Murray, B. J., 2018, "Coarse-Mode Mineral Dust Size Distributions, Composition and Optical Properties From AER-D Aircraft Measurements Over the Tropical Eastern Atlantic," Atmos. Chem. Phys., **18**(23), pp. 17225–17257.
[2] Nickovic, S., Vukovic, A., Vujadinovic, M., Djurdjevic, V., and Pejanovic, G., 2012, "Technical Note: High-Resolution Mineralogical Database of Dust-Productive Soils for Atmospheric Dust Modeling," Atmos. Chem. Phys., **12**(2), pp. 845–855.
[3] Formenti, P., Schütz, L., Balkanski, Y., Desboeufs, K., Ebert, M., Kandler, K., Petzold, A., Scheuvens, D., Weinbruch, S., and Zhang, D., 2011, "Recent Progress in Understanding Physical and Chemical Properties of African and Asian Mineral Dust," Atmos. Chem. Phys., **11**(16), pp. 8231–8256.
[4] Jugder, D., Shinoda, M., Sugimoto, N., Matsui, I., Nishikawa, M., Park, S. U., Chun, Y. S., and Park, M. S., 2011, "Spatial and Temporal Variations of Dust Concentrations in the Gobi Desert of Mongolia," Global Planet. Change, **78**(1–2), pp. 14–22.
[5] Suman, A., Casari, N., Fabbri, E., Pinelli, M., Di Mare, L., and Montomoli, F., 2019, "Gas Turbine Fouling Tests: Review, Critical Analysis, and Particle Impact Behavior Map," ASME J. Eng. Gas Turbines Power, **141**(3), p. 032601.
[6] Krämer, S., Yang, J., Levi, C. G., and Johnson, C. A., 2006, "Thermochemical Interaction of Thermal Barrier Coatings With Molten CaO-MgO-Al 2O 3-SiO 2 (CMAS) Deposits," J. Am. Ceram. Soc., **89**(10), pp. 3167–3175.
[7] Mechnich, P., Braue, W., and Schulz, U., 2011, "High-Temperature Corrosion of EB-PVD Yttria Partially Stabilized Zirconia Thermal Barrier Coatings With an Artificial Volcanic Ash Overlay," J. Am. Ceram. Soc., **94**(3), pp. 925–931.
[8] Krisak, M. B., Bentley, B. I., Phelps, A. W., and Radsick, T. C., 2017, "Review of Calcium Sulfate as an Alternative Cause of Hot Corrosion," J. Propul. Power, **33**(3), pp. 697–703.
[9] Levy, M., Farrell, P., and Pettit, F., 1986, "Oxidation of Some Advanced Single-Crystal Nickel-Base Superalloys in Air at 2000 F(1093 C)," Corrosion, **42**(12), pp. 708–717.
[10] Pettit, F. S., and Meier, G. H., 1984, "Oxidation and Hot Corrosion of Superalloys," Superalloys 1984 (Fifth International Symposium), Seven Springs Mountain Resort, Champion, PA, Oct. 7–11.
[11] Jianting, G., Ranucci, D., and Picco, E., 1983, "Low Cycle Fatigue Behaviour of Cast Nickel-Base Superalloy IN-738LC in Air and in Hot Corrosive Environments," Mater. Sci. Eng., **58**(1), pp. 127–133.
[12] de Wet, D. J., Taylor, R., and Stott, F. H., 1993, "Corrosion Mechanisms of ZrO_2-Y_2O_3 Thermal Barrier Coatings in the Presence of Molten Middle-East Sand," Le J. Phys. IV, **3**(C9), pp. 655–663.
[13] Smialek, J. L., Archer, F. A., and Garlick, R. G., 1994, "Turbine Airfoil Degradation in the Persian Gulf War," J. Miner. Met. Mater. Soc., **46**(12), pp. 39–41.
[14] Borom, M. P., Johnson, C. A., and Peluso, L. A., 1996, "Role of Environmental Deposits and Operating Surface Temperature in Spallation of Air Plasma Sprayed Thermal Barrier Coatings," Surf. Coat. Technol., **86–87**(Part 1), pp. 116–126.
[15] Braue, W., 2009, "Environmental Stability of the YSZ Layer and the YSZ/TGO Interface of an In-service EB-PVD Coated High-Pressure Turbine Blade," J. Mater. Sci., **44**(7), pp. 1664–1675.
[16] Osborn, E. F., Gee, K. H., Muan, A., Roeder, P. L., and Ulmer, G. C., 1969, *Studies of Phase Equilibria in the Systems: CaO-MgO-Al2O3-TiO2-SiO2, Bulletin 85*, Pennsylvania State University, pp. 1–80.
[17] Phelps, A. W., and Pfledderer, L. M., 2014, "Development of a Naturalistic Test Media for Dust Ingestion Cmas Testing of Gas Turbine Engines," Engineering

Conferences International—Thermal Barrier Coatings IV, Irsee, Germany, June 22–27.
[18] 2016, "ISO 12103-1:2016. Road Vehicles—Test Contaminants for Filter Evaluation—Part 1: Arizona Test Dust."
[19] Dunn, M. G., Padova, C., and Adams, R., 1987, *Operation of Gas Turbine Engines in Dust-Laden Environments*, Calspan Advanced Technology Centre, Buffalo, NY.
[20] Nieto, A., Walock, M., Ghoshal, A., Zhu, D., Gamble, W., Barnett, B., Murugan, M., Pepi, M., Rowe, C., and Pegg, R., 2018, "Layered, Composite, and Doped Thermal Barrier Coatings Exposed to Sand Laden Flows Within a Gas Turbine Engine: Microstructural Evolution, Mechanical Properties, and CMAS Deposition," Surf. Coat. Technol., **349**, pp. 1107–1116.
[21] ACI World, 2019, "Prelimary World Airport Traffic Rankings Released," ACI Media Releases [Online], https://aci.aero/news/2019/03/13/preliminary-world-airport-traffic-rankings-released/, Accessed on 21 January 2020.
[22] Engelbrecht, J. P., and Derbyshire, E., 2010, "Airborne Mineral Dust," Elements, **6**(4), pp. 241–246.
[23] Ghenaiet, A., 2012, "Study of Sand Particle Trajectories and Erosion Into the First Compression Stage of a Turbofan," ASME J. Turbomach., **134**(5), p. 051025.
[24] Kim, J., Dunn, M. G., Baran, A. J., Wade, D. P., and Them, E. L., 1992, "Deposition of Volcanic Materials in the Hot Sections of Two Gas Turbine Engines," ASME 1992 International Gas Turbine and Aeroengine Congress and Exposition Volume 3: Coal, Biomass and Alternative Fuels; Combustion and Fuels; Oil and Gas Applications; Cycle Innovations, ASME, p. 12.
[25] Allibert, M., Gaye, H., Geisler, J., Janke, D., Keene, B. J., Kirner, D., Kowalski, M., Lehmann, J., Mills, K. C., Neuschutz, D., Parra, R., Saint Jours, C., Spencer, P. J., Susa, M., Tmar, M., and Woermann, E., 1995, *Slag Atlas*, 2, Verlag Stahleisen GmbH, Dusseldorf.
[26] Cavalier, G., and Sandreae-Deudon, M., 1960, "Laitiers Quaternaires CaO-MgO-Al2O3-SiO2 : Température de Cristallisation Commençante et Champs de Cristallisation Sur Plans a Magnésie Constante," Rev. Met. Paris, **57**(12), pp. 1143–1157.
[27] West, R. R., and Sutton, W. J., 1954, "Thermography of Gypsum," J. Am. Ceram. Soc., **37**(5), pp. 221–224.
[28] Grossman, L., 1975, "Petrography and Mineral Chemistry of Ca-Rich Inclusions in the Allende Meteorite," Geochim. Cosmochim. Acta, **39**(4), pp. 433–454.
[29] Gee, L. L., and Sack, R. O., 1988, "Experimental Petrology of Melilite Nephelinites," J. Petrol., **29**(6), pp. 1233–1255.
[30] Stolper, E., 1982, "Crystallization Sequences of Ca-Al-Rich Inclusions From Allende: An Experimental Study," Geochim. Cosmochim. Acta, **46**(11), pp. 2159–2180.
[31] Melluso, L., Morra, V., and Di Girolamo, P., 1996, "The Mt. Vulture Volcanic Complex (Italy): Evidence for Distinct Parental Magmas and for Residual Melts With Melilite," Mineral. Petrol., **56**(3–4), pp. 225–250.
[32] Wiesner, V. L., and Bansal, N. P., 2014, "Crystallization Kinetics of Calcium-Magnesium Aluminosilicate (CMAS) Glass," Surf. Coat. Technol., **259**(PC), pp. 608–615.
[33] Krämer, S., Faulhaber, S., Chambers, M., Clarke, D. R., Levi, C. G., Hutchinson, J. W., and Evans, A. G., 2008, "Mechanisms of Cracking and Delamination Within Thick Thermal Barrier Systems in Aero-engines Subject to Calcium-Magnesium-Alumino-Silicate (CMAS) Penetration," Mater. Sci. Eng. A, **490**(1–2), pp. 26–35.
[34] Pettit, F., 2011, "Hot Corrosion of Metals and Alloys," Oxid. Met., **76**(1–2), pp. 1–21.
[35] Leys, J. F., Heidenreich, S. K., Strong, C. L., McTainsh, G. H., and Quigley, S., 2011, "PM10 Concentrations and Mass Transport During ' Red Dawn'—Sydney 23 September 2009," Aeolian Res., **3**(3), pp. 327–342.